ACS APPLIED ENERGY MATERIALS

www.acsaem.org Article

Metal-Free Interconnecting Layer for Monolithic Perovskite/Organic Tandem Solar Cells with Enhanced Outdoor Stability

Han Xu,[‖] Luis Torres Merino,[‖] Mehmet Koc, Erkan Aydin, Shynggys Zhumagali, Md Azimul Haque, Aren Yazmaciyan, Anirudh Sharma, Diego Rosas Villalva, Luis Huerta Hernandez, Michele De Bastiani, Maxime Babics, Furkan H. Isikgor, Joel Troughton,* Stefaan De Wolf, Selcuk Yerci, and Derya Baran*

Cite This: *ACS Appl. Energy Mater.* 2022, 5, 14035−14044 Read Online

ACCESS | Metrics & More | Article Recommendations | Supporting Information

ABSTRACT: Photovoltaics with monolithically connected tandem architectures have the potential to achieve high efficiencies owing to enhanced spectral absorption and reduced thermal losses. To achieve this, photoactive layers with complementary absorption and interconnecting layers, which are robust, transparent, and energetically suitable, are essential. Here, we investigate a strategy to create an efficient, highly transparent, ohmic, and chemically robust interconnecting layer based on atomic layer-deposited tin oxide (SnO_2) and solution-processed diluted poly(3,4-ethylenedioxythiophene):polystyrene sulfonate (PEDOT:PSS), eliminating the need of widely reported parasitically absorbing metal recombination layers. Monolithic perovskite/organic tandem devices built on a metal-free interface (SnO_2/PEDOT:PSS) compared to its counterpart (SnO_2/metal/PEDOT:PSS) show no significant difference in PCE, but a remarkable enhancement in photostability. Furthermore, tandem solar cells were tested under outdoor conditions for 2 weeks, showing improved stability and solar power conversion than single-junction perovskite and organic devices, underscoring the potential of monolithic tandem solar cells.

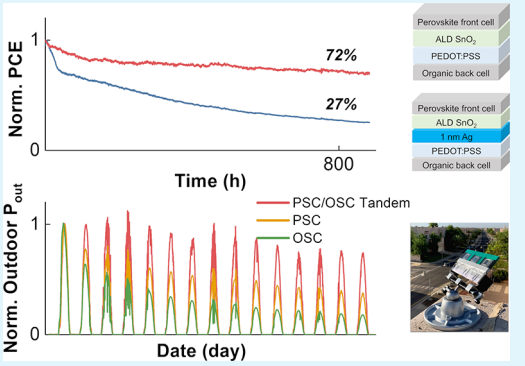

KEYWORDS: *tandem solar cell, interconnecting layer, photostability, outdoor testing, perovskite tandem*

1. INTRODUCTION

Although the power conversion efficiency (PCE) of halide perovskite solar cells (PSC) and organic solar cells (OSC) has been steadily increasing during recent years,[1] the Shockley−Queisser (S−Q) limit prohibits PCEs in excess of 33% for single junctions.[2,3] To overcome the S−Q limit by minimizing thermalization losses, multi-junction tandem solar cells which combine two or more different band gap sub-cells have been widely explored.[4,5] Monolithic tandems have low internal reflection losses owing to minimal interconnecting layers (ICL) between two sub-cells which minimizes the coating/printing efforts and potentially lower the cost.[6,7] As for the material combinations for sub-cells in monolithic tandems, an optimal selection is desired to achieve both performance and stability (which is often disregarded). Although there are several perovskite material combinations for front sub-cells, back sub-cells in all-perovskite monolithic tandems are limited to using narrow band gap tin (Sn) based perovskites which are air sensitive and highly reactive due to the oxidation of Sn^{2+} to Sn^{4+}.[8−13] This intrinsic material property issue frustrates the ease of fabrication of such devices and limits their operational stability under ambient and outdoor conditions. Organic photoactive layers, on the contrary, offer processing under ambient conditions,[14−18] show promising device performances with tunable and ultralow band gaps,[19−24] and are shown to be stable under operational conditions.[25−29] Hence, using a combination of a wide band gap perovskite front cell, and a narrow band gap organic back cell to fabricate perovskite/organic monolithic tandem could be a solution to achieving efficient and stable solar cells.[30−36]

The design of ICL, the layer that connects the two sub-cells, is a challenging task when fabricating monolithic tandem solar cells.[37−40] An efficient ICL should possess the following properties: (i) high optical transparency or optical redistribution to reduce parasitic optical losses, (ii) ability to form ohmic contact between sub-cells and maintain balanced carrier recombination to ensure open-circuit voltage (V_{OC}) addition and reduce fill factor losses, and (iii) high resistance to solvent permeability when using non-orthogonal solvents. Currently, the main materials used for ICLs in the most efficient monolithic tandems are sputtered indium−tin oxide (ITO) and atomic layer-deposited (ALD) tin oxide (SnO_2).[6,41−44] When using

Received: August 15, 2022
Accepted: October 28, 2022
Published: November 9, 2022

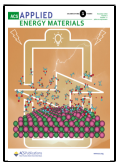

https://doi.org/10.1021/acsaem.2c01749
ACS Appl. Energy Mater. 2022, 5, 14035−14044

sputtered ITO, thick buffer layers are needed to protect the front cell from high-energy ions generated during sputter deposition.[45] These thick layers lead to parasitic optical losses impairing the tandem's overall efficiency. ALD-deposited SnO_2 provides an outstanding platform to form efficient ICLs given its highly conformal coating on the underlying surface.[46,47] A very thin metal recombination layer of gold (Au) or silver (Ag) is typically used to improve the ohmic contact.[43,48,49] However, the presence of this metal layer can limit the short circuit current (J_{SC}) of the tandem devices due to parasitic losses. Moreover, the commonly used Ag combined with PEDOT:PSS for extracting holes generated from the back cell, could cause corrosion[50,51] and result in unstable devices. Recently, Brinkmann et al. introduced an indium oxide interlayer to replace the silver thin layer and achieved excellent efficiency, which emphasized the urgent need for a metal-free interconnecting layer in a tandem structure.[52]

In this work, we investigate highly transparent interconnecting layers based on ALD-deposited SnO_2 films and diluted PEDOT:PSS to understand the impact of a metal-free ICL on perovskite ($FA_{0.8}Cs_{0.2}Pb(Br_{0.4}I_{0.6})_3$)/organic (PTB7-Th:IEICO-4F) monolithic tandem performance and both photostability and outdoor operational stability. We use a wide band gap (WBG) perovskite (1.78 eV) as the front cell, where double cation formamidinium (FA)/cesium (Cs) provides a balance between efficiency and stability in comparison to methylammonium (MA)/Cs due to the higher volatility of MA.[53] The perovskite layer could also serve as a UV filter to the organic back cell, which would impact photostability.[54−56] Non-polar solvents and no thermal annealing treatment are used in organic back cell fabrication, preventing damage to the front cell.[6,43,57,58] The champion device with metal-free ICL gives 17.6% PCE, similar to the 0.5 nm (18.0% PCE) and 1 nm Ag (17.4% PCE) tandems. Moreover, stability tests under continuous simulated illumination (>800 h) and real-world outdoor conditions (average 32 °C) are conducted to demonstrate the great potential of monolithic PSC/OSC tandem devices with metal-free ICL.

2. EXPERIMENTAL DETAILS

2.1. Materials. The 10 Ω/sq pattern Indium−tin oxide (ITO) glass was obtained from Xinyan Technology Ltd. PEDOT:PSS (Clevios PVP Al4083) was purchased from Heraeus. PTB7-Th, IEICO-4F, and PFN-Br were purchased from 1-Material Inc. Chlorobenzene, 1-chloronaphthalene, methanol, and isopropyl alcohol were bought from Sigma-Aldrich Inc. 2PACz was obtained from TCI. Ag was gained from Kurt J. Lesker Company. Precursors and solvent for the perovskite: CsI from Alfa Aesar, FAI was obtained from Greatsolar, PbI_2 and $PbBr_2$ anhydrous beads, dimethyl sulfoxide, dimethylformamide, and chlorobenzene were obtained from Sigma-Aldrich.

2.2. Device Fabrication and Characterization. *2.2.1. Organic Single-Junction Device Fabrication.* ITO substrates were cleaned using an ultrasonic bath with detergent water, deionized water, acetone, and isopropyl alcohol (IPA) sequentially for 10 min each. The residue solvent was dried by clean air blowing. Afterward, a diluted PEDOT:PSS was spin-coated on top of the ITO substrate at 4000 rpm for 40 s and annealed at 105 °C for 30 s in the air. The PEDOT:PSS was prepared from PEDOT:PSS and anhydrous IPA (1:9, v/v). The substrates were transferred to the nitrogen glovebox right after the baking process for further photoactive layer deposition. The photoactive layer solution with a concentration of 25 mg/mL was prepared from PTB7-Th:IEICO-4F (1:1.5, w/w) in chlorobenzene:1-chloronaphthalene (96:4, v/v) solvent and stirred at 80 °C for 2 h. The spin coating process was executed at 1800 rpm for 65s to yield a film thickness of 130 nm. Then, a thin layer of PFN-Br (0.75 mg/mL in methanol) was spin-coated at 3000 rpm for 30 s on the photoactive layer. Finally, a 100 nm Ag was evaporated under reduced pressure (<2 × 10^{-6} Torr) to finish the device fabrication process, resulting in a device area of 0.1 cm^2. To reduce the reflection of ITO glass, an antireflective layer (MgF_2, 100 nm) was evaporated on the other side of the solar cell. The whole device was then encapsulated by combining 18 mm × 18 mm glass cover with lens bond optical cement type J-91 (EMS Summers Optical) under 5 min UV-treatment.

2.2.2. Perovskite Single-Junction Device Fabrication. To prepare the perovskite solution, PbI_2, $PbBr_2$, CsI and FAI were mixed in 4:3 DMF/DMSO at 1.1 M and stirred overnight. 1 mM 2PACz solution was dissolved in ethanol and ultrasonicated for 15 min. The ITO cleaning procedure was the same as for the organic single-junction devices. After cleaning, the substrates were ozone plasma treated for 15 min and transferred inside the glovebox at <0.1 ppm of H_2O and O_2 under constant purging. The 2PACz solution was then spin-coated at 3000 rpm for 30 s and then annealed at 100 °C for 10 min. The perovskite was spin coated at 4000 rpm for 30 s on top. After 20 s, 80 μL of antisolvent (chlorobenzene) was dropped and then annealed for 25 min at 100 °C. The substrates were kept under a nitrogen atmosphere and transferred to the evaporator where a C_{60} film of 7 nm from Nano-C was deposited at a rate of 0.1 Å/s followed by a 3 nm film of BCP from Sigma-Aldrich at a rate of 0.1 Å/s. Then, 100 nm of Ag was deposited at a rate of 0.2 Å/s for the first 10 nm and 3 Å/s for the rest 90 nm. The whole device was then encapsulated as mentioned before.

2.2.3. ICL Stack Fabrication. ITO substrate was cleaned as the single-junction fabrication. By the thermal atomic layer deposition technique, 20 nm SnO_2 was deposited on top of ITO making use of 140 alternate cycles of tetrakis(dimethylamino)tin and H_2O precursors with a deposition temperature of 100 °C. Then, Ag with different thicknesses were thermal evaporated onto the SnO_2 layer under vacuum. After coating PEDOT:PSS on top, 100 nm of gold was further thermal evaporated to finish the device.

2.2.4. Hybrid Tandem Device Fabrication. The perovskite bottom cell was prepared using a similar method in a single-junction device until the C_{60} electron transport layer. Instead of BCP/Ag, 20 nm SnO_2 was deposited by ALD and then thin layers of Ag with different thicknesses were evaporated under reduced pressure. After that, the PEDOT:PSS/active layer/PFN-Br/Ag was coated under the same conditions as the organic single-junction fabrication. Finally, a 100 nm MgF_2 was evaporated on the other side of the cell and the whole device was then encapsulated as mentioned before.

2.2.5. Instruments and Measurement. The *J*−*V* curves of the above devices were obtained from a Keithley 2400 source meter under simulated AM 1.5G illumination via a WAVELABS SINUS-220 solar simulator in air. The EQE spectra were carried out using an integrated system from Enlitech, Taiwan. For tandem solar cells, a light source with filters for short pass and long pass below 550 nm and beyond 700 nm are used to gain bias light to saturate the sub-cells.

2.2.6. Device Stability Testing. For simulated light soaking experiments, both tandem and single-junction solar cells were held under a bank of metal halide discharge lamps (Osram Powerstar HQI, 900W total) with a light intensity of ∼1 sun. A 400 nm UV cutoff filter was placed between the cells and the light source. Cell temperature was maintained at 30 °C using a water-cooled baseplate. The *J*−*V* curves of each cell and tandem were measured at 10-min intervals at 50 mV/s in the "reverse" scan direction (V_{OC} to J_{SC}) using a multi-channel source-measure unit based on the open-source "μSMU" (https://certification.oshwa.org/sa000002.html) calibrated against a Keithley 2400 SMU. In-between *J*−*V* scans, tandem devices were held at their maximum power point as determined by the last *J*−*V* scan, whereas single-junction devices were held at open-circuit between measurements. For outdoor measurements, cells were encapsulated within two tempered glasses for standard photovoltaics module manufacturing. The packaging is secured via vacuum lamination (Ecolam05, Ecoprogetti). To provide a strong barrier against moisture permeation, butyl rubber (HelioSeal PVS101) is embedded at the edges during the lamination process. Prior to the lamination, the device contacts are tabbed by copper ribbons, and secured with silver paste (Kyoto). Finally, a layer of silicone is spread around the tandem as edge sealant to avoid moisture percolation

https://doi.org/10.1021/acsaem.2c01749
ACS Appl. Energy Mater. 2022, 5, 14035−14044

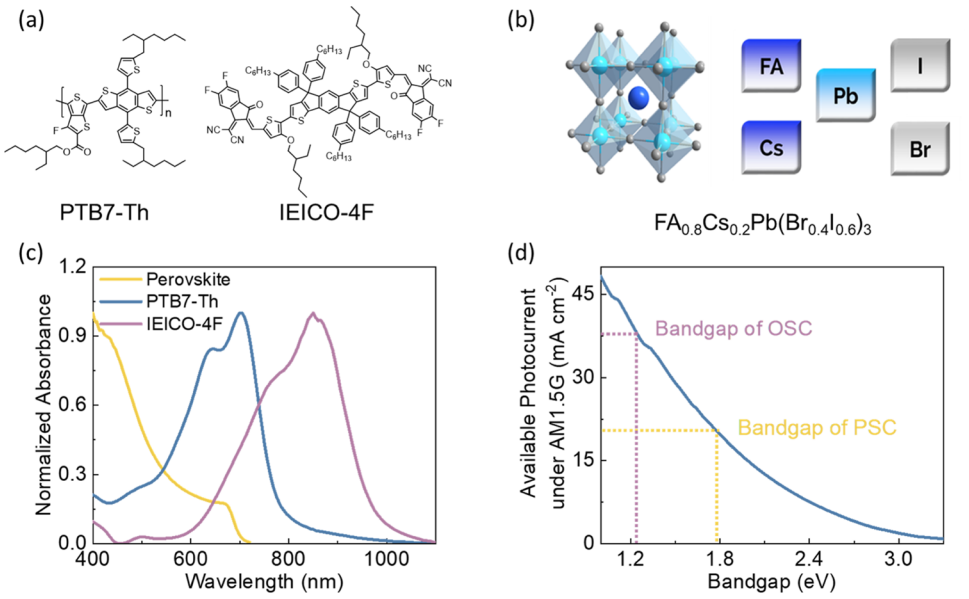

Figure 1. (a) Chemical structures of PTB7-Th and IEICO-4F. (b) Crystal structure of $FA_{0.8}Cs_{0.2}Pb(Br_{0.4}I_{0.6})_3$. (c) The absorption spectra of PTB7-Th, IEICO-4F and perovskite films. (d) Theoretically available photocurrent under AM 1.5G illumination as a function of the absorber band gap.

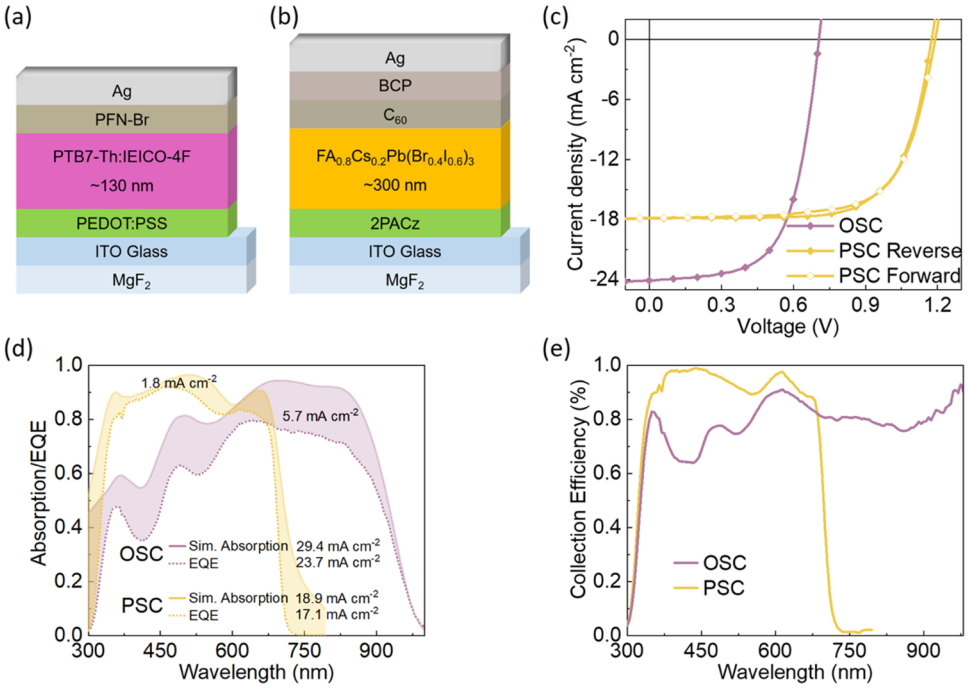

Figure 2. (a, b) Device stacks of OSC and PSC single-junction devices, respectively. (c) *J*−*V* hysteresis curves for OSC and PSC. (d) Simulated absorption in PTB7-Th:IEICO-4F (pink) and $FA_{0.8}Cs_{0.2}Pb(Br_{0.4}I_{0.6})_3$ (yellow) (solid line) and measured (dotted line) EQE spectra of their single-junction devices. (e) Calculated collection efficiency spectra for OSC and PSC single-junction devices.

through the tabbed contact. Encapsulated cells were mounted on a rooftop at LAT 22.319, LONG 39.107 with a clear view of the sky without shadowing. Cell angle and azimuth were 45 and 20° respectively. Similar to light soaking experiments, cells had *J*−*V* curves measured at 10-min intervals using a multi-channel source-measure unit, with maximum power point being maintained between measurements. Environmental data were gathered using a MLU-recordum Airpointer weather station.

2.3. Instrumental Analysis. *2.3.1. Optical Simulation.* The optical response of the solar cells, including absorptions in the individual layers and reflection, are computed with the transfer matrix method. Calculated collection efficiency is calculated by dividing the measured EQE by the calculated light absorption in the absorber layers. Complex optical properties (n and k) of glass, perovskite with different Br content, SnO_2, C_{60}, MgF_2, and PTB7-Th are obtained with variable-angle spectroscopic ellipsometry measurements (WVASE32 ellipsometry from J. A. Woollam Co., Inc.) with a spectral range from 300 to 1700 nm. UV−Vis transmittance and reflectance spectra were taken from a PerkinElmer Lambda 950. Refractive indices of PEDOT:PSS and ITO are adapted from the previously reported study.[60]

2.3.2. UPS/LEIPES. UPS measurements were performed in an ultrahigh vacuum chamber equipped with a Sphera II EAC 125 7-channeltron electron analyzer calibrated with the Fermi edge of clean polycrystalline silver. The spectra were recorded using the He I line (excitation energy of 21.22 eV) at a pass energy of 10 eV, with −10 eV of an external bias.

https://doi.org/10.1021/acsaem.2c01749
ACS Appl. Energy Mater. 2022, 5, 14035−14044

Table 1. Photovoltaic Parameters of Single-Junction Devices[a]

photoactive layer	J_{SC} [mA cm^{-2}]	V_{OC} [V]	fill factor [%]	PCE [%]
PTB7-Th:IEICO-4F	24.9 (24.6)	0.71 (0.71)	62.8 (62.8)	11.1 (10.9)
$FA_{0.8}Cs_{0.2}Pb(Br_{0.4}I_{0.6})_3$	18.1 (17.9)	1.18 (1.16)	67.1 (63.6)	14.3 (13.0)

[a]Parentheses shows the average value calculated from 15 devices per variation.

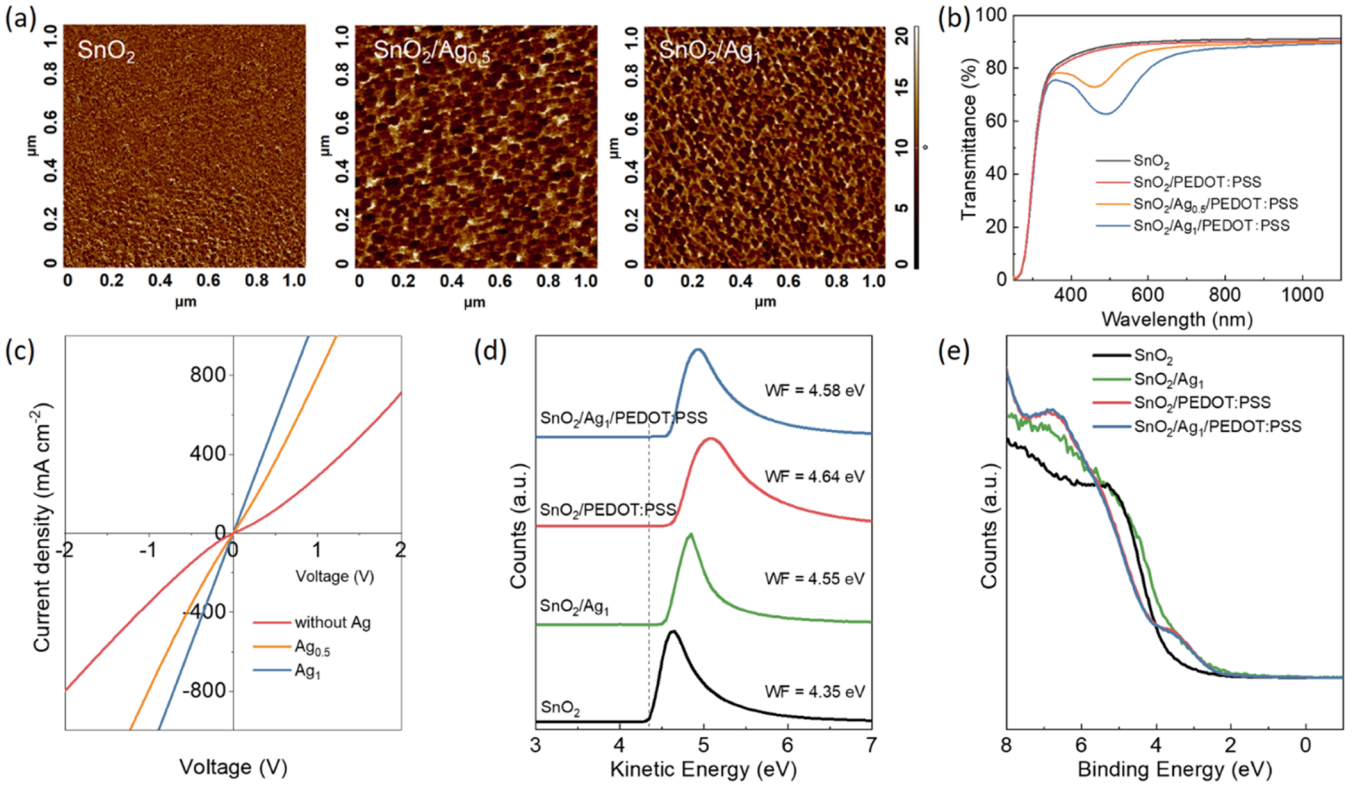

Figure 3. (a) AFM phase images from the two different Ag deposits ($Ag_{0.5}$ and Ag_1), showing a cluster-like morphology. (b) Transmittance of the three different SnO_2 interfaces (PEDOT:PSS, $Ag_{0.5}$/PEDOT:PSS and Ag_1/PEDOT:PSS) and SnO_2 on bare glass. (c) Current−voltage response in the dark of the devices using ITO/SnO_2/(without Ag, $Ag_{0.5}$ or Ag_1)/PEDOT:PSS/Au architecture. (d) Secondary electron cutoff and (e) valence region of the UP spectra showing the change in the work function and electronic states in the valence regions respectively, for different ICL stacks.

2.3.3. Atomic Force Microscope Measurement. AFM topography and phase images were recorded in semi-contact mode using a Next-Solve AFM by MD-NDT using a TESP-SS cantilever from Bruker (nominal tip radius is 2 nm).

3. RESULTS AND DISCUSSION

The chemical structures of the polymer donor, PTB7-Th, and the small molecule acceptor, IEICO-4F, utilized in the back cell are shown in Figure 1a as well as a schematic perovskite crystal structure with the formation formula of $FA_{0.8}Cs_{0.2}Pb(Br_{0.4}I_{0.6})_3$ in Figure 1b. Normalized absorption spectra of the organic and perovskite films are presented in Figure 1c, and the organic blend in Figure S1. The organic blend has a wide absorption band extending to 1000 nm from which we determined the band gap to be 1.24 eV. The calculated band gap of perovskite via Tauc plot is 1.78 eV, shown in Figure S2. Figure 1d shows the amount of theoretically available photocurrent under AM 1.5G illumination as a function of the absorption band gap.[44] Ideally half of the maximum available photocurrent that is defined by the band gap of OSC should be the tandem photocurrent (19 mA cm^{-2}) which is close to that of PSC (20 mA cm^{-2} for E_g = 1.78 eV), representing a good current match for PSC-OSC tandem solar cells from the perspective of band gap.

OSCs based on PTB7-Th:IEICO-4F were fabricated with a conventional (p-i-n) structure (Figure 2a). The PSC single-junction stack structure using the $FA_{0.8}Cs_{0.2}Pb(Br_{0.4}I_{0.6})_3$ composition is shown in Figure 2b. We incorporated a transparent self-assembled monolayer [2-(9H-carbazol-9-yl)-ethyl]phosphonic acid (2PACz)[59] as hole transport layer to further improve optical properties. The current density−voltage (J−V) curves of OSC and PSC champion devices are shown in Figure 2c, giving 11.1 and 14.3% PCE, respectively. Device parameters are summarized in Table 1, and the performance distribution figures are shown in Figure S3. Figure 2d shows both the measured (dotted lines) external quantum efficiency (EQE) and the simulated (solid lines) absorption spectra of OSC and PSC single-junction devices. The simulated absorption spectrum was obtained by calculating the absorbance spectra of photoactive layers (perovskite and organic blend) using the measured complex optical constants of each layer constituting the tandem solar cell, and considering that the internal quantum efficiency (IQE) is 100%. The shaded area represents the collection losses existing in the real device. The calculated current loss of PSC single-junction is 1.8 mA cm^{-2}, which is much lower than that of OSC, 5.7 mA cm^{-2}. To evaluate the collection losses at each wavelength, we calculated the collection efficiency of both single junctions, derived from

https://doi.org/10.1021/acsaem.2c01749
ACS Appl. Energy Mater. 2022, 5, 14035−14044

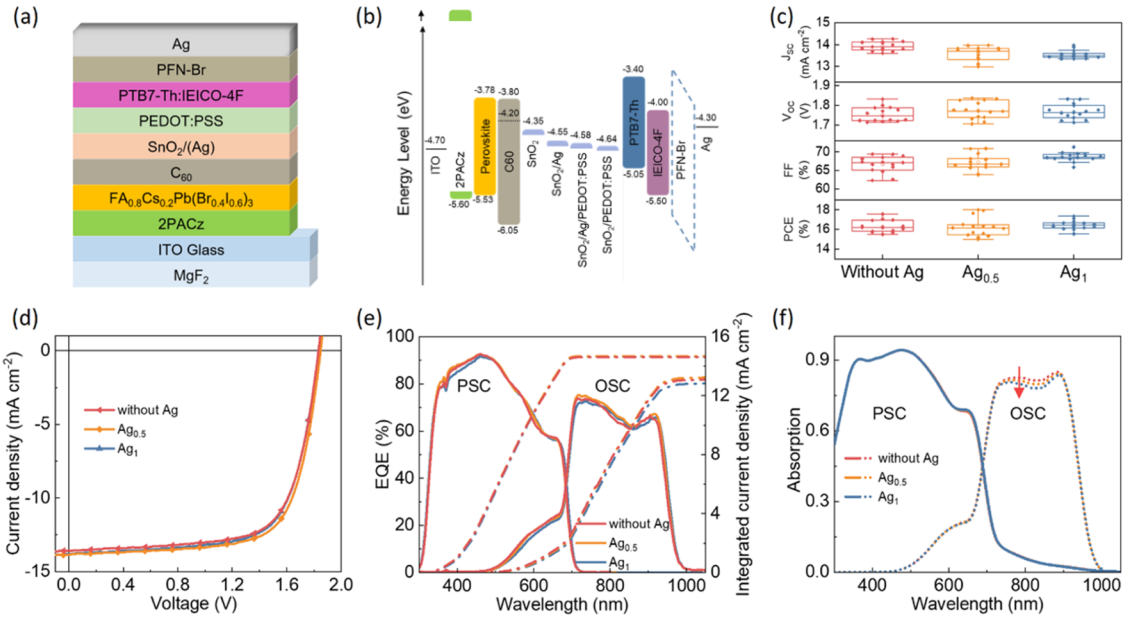

Figure 4. (a) Perovskite/organic monolithic tandem stack. (b) Energy diagram of the tandem stack obtained from PESA, Tauc plot, and UPS studies. (c) Box plots of tandem performance under 1 sun at AM 1.5G of three different ICL (without Ag $Ag_{0.5}$ and Ag_1) devices. (d) $J-V$ curves of the champion devices for each tandem stack. (e) EQE spectra and the cumulative current density of the champion tandem devices. (f) Simulated PSC and OSC sub-cell absorption spectra in the tandem structure with different ICLs.

the ratio of the measured EQE and calculated absorption, shown in Figure 2e. In the visible range (300−700 nm), PSC shows much higher collection efficiency (>90%) than OSC (65−90%). This implies in a wide band gap perovskite/low band gap organic tandem configuration, the photons in such range will mostly be absorbed and converted by the front perovskite sub-cell, leading to a reduced electro-optical loss compared to OSC single-junction devices.

Current matching of sub-cells in monolithic tandems is critical. Simulated current-matched maximum achievable photogenerated current (MAPC) density as a function of OSC and PSC active layer thicknesses is shown in Figure S4. The thickness of the perovskite layer can be selected with multiple options due to favorable interferences in its single-junction configuration;[60] however, current matching conditions in the tandem structure forces thinner perovskite layers for transparency. Thus, combining 250 nm PSC and 150 nm OSC shows the highest current density. To achieve such thicknesses, different concentrations of perovskite solutions for deposition were tested and optimized as 1.1 M to yield an optimized layer of 300 nm. Further reducing the concentration of perovskite to achieve thinner photoactive layers resulted in pinholes and poor crystal growth (Figure S5). Such a perovskite layer needs to be matched with an organic back sub-cell thickness of around 130−140 nm (Figure S6).

ICL is the heart of a monolithic tandem device. Photoinduced electrons within the perovskite absorber are extracted by the incorporated n-type transport layers of 7 nm-thick fullerene (C_{60}) and 20 nm-thick SnO_2. On the other side, photogenerated holes from the organic blend are collected through a p-type transport layer of 10 nm-thick PEDOT:PSS. These electrons and holes from the perovskite and organic sub-cell must effectively recombine at the n-type/p-type interface for an efficient tandem device operation. It has been widely reported that an additional thin (1 nm) Ag layer can enhance the ohmic contact in the ICL[43,48,49] at the expense of a degree of optical transmission. To examine our metal-free SnO_2/PEDOT:PSS ICL behavior, we investigated two different thicknesses for the Ag layer in-between SnO_2 and PEDOT:PSS as a comparison. A metal deposition time of 170 s at 0.03 Å/s rate corresponded to a quartz crystal monitor-indicated thickness of 0.5 nm, and a 330-s deposition time to an indicated 1 nm Ag layer. By examining the morphology of the evaporated Ag layers on SnO_2, we found that the atomic force microscopy (AFM) micrographs show clusters of metals rather than a continuous film, shown in Figure 3a. Given the non-uniformity of the thin evaporated Ag layers, we will describe the two Ag "films" by $Ag_{0.5}$ and Ag_1 representing the evaporation time of 170 and 330 s, respectively. As expected, transmittance is significantly reduced in the range of 350−850 nm (Figure 3b) upon deposition of Ag, even as small as $Ag_{0.5}$ and Ag_1. This parasitic absorption by the thin Ag layer would adversely affect the current generated by the organic sub-cell. Since we have already revealed that the collection efficiency of the organic sub-cell falls behind the perovskite, such absorption is undesirable.

The linear relation in the dark current−voltage response of the ITO/ICL/Au stack confirms the ohmic behavior. Figure 3c shows dark $J-V$ curves of such devices with the different thicknesses of Ag (ITO/SnO_2/(without Ag, $Ag_{0.5}$, or Ag_1)/PEDOT:PSS/Au). By comparing the slope of the $J-V$ curves, it can be seen that the ohmic contact is improved by increasing the thickness of Ag on SnO_2. To further understand the ohmic behavior of ICL, we used Kelvin probe force microscopy (KPFM) measurements to see the work function (WF) changes by additional Ag layers on top of SnO_2. As shown in Figure S7, both $Ag_{0.5}$ and Ag_1 can enhance the WF similar to the surface of SnO_2. To corroborate the changes in WF further PEDOT:PSS layer is deposited, we characterized the SnO_2 thin film surface with and without Ag deposition, using ultraviolet photoelectron spectroscopy (UPS). The WF of ALD-deposited SnO_2 was found to be 4.35 eV and the valence band (rel. to Fermi level) was found at 3.7 eV, resulting in an ionization energy (IE) of

https://doi.org/10.1021/acsaem.2c01749
ACS Appl. Energy Mater. 2022, 5, 14035−14044

8.05 eV (Figure 3d). Deposition of Ag_1 on the SnO_2 surface resulted in a 0.2 eV increase in the work function to 4.55 eV, with additional electronic states appearing at around 3 eV in the valence region. On the other hand when a thin layer of PEDOT:PSS was further deposited over the SnO_2-Ag surface an almost unchanged (within an experimental uncertainty of ±0.05 eV) WF of 4.58 eV was found, compared to a WF of 4.64 eV for a SnO_2-PEDOT:PSS surface. Moreover, additional electronic states of ∼ 3 eV were also observed when PEDOT:PSS was deposited over the SnO_2 surface, independent of the presence of a thin Ag layer. Since the electronic states in the valence region contribute to charge transport, SnO_2 with a thin PEDOT:PSS layer is expected to have comparable electrical properties as its counterpart with a thin Ag layer. It can thus be concluded that the presence of metal clusters between SnO_2 and PEDOT:PSS has no significant impact on the resultant WF of such interfaces, and they could well be replaced only with a PEDOT:PSS layer. Owing to the similar additional electronic states, SnO_2/PEDOT:PSS ICL is still suitable for carrier recombination in monolithic tandems compared to Ag including ICLs.

We fabricated monolithic tandem devices using three different ICL variations: without Ag, $Ag_{0.5}$, and Ag_1 deposition between SnO_2 and PEDOT:PSS, to investigate their impact on solar cell performance and stability. A representative tandem stack and energy diagrams are shown in Figure 4a,b, respectively. As presented in the absorption distribution profiles of tandems with different ICLs (Figure S8), most visible photons are absorbed by the perovskite layer and the non-absorbed photons from 500 to 700 nm transmit through the ICL and are utilized by the organic photoactive layer. The n and k values of respective layers extracted from ellipsometry measurements are disclosed in Figures S9 and S10. Figure 4c summarizes box plots of photovoltaic parameters of tandem devices exploiting different ICL stacks, and the device performance statistics are shown in Table 2. No statistically significant change in V_{OC} or FF is observed depending on the ICL (without or with different thicknesses of Ag), which indicates that the absence of Ag in ICL does not harm the formation of a good ohmic contact when connecting two sub-cells. The J_{SC} value is slightly increased with the removal of Ag owing to higher transparency. Upon $Ag_{0.5}$ deposition, we achieved a tandem performance of 1.84 V V_{OC}, 13.8 mA cm^{-2} J_{SC}, and 70.5% FF resulting in 18.0% PCE. Further, Ag_1 and the metal-free ICL-based champion tandems reached 17.4 and 17.6% PCE, respectively, evidencing that the existence of Ag does not have a dramatic impact on the tandem efficiency. The $J-V$ curves of these three champion devices are shown in Figure 4d. A very low degree of $J-V$ hysteresis was observed in all three tandem devices (Figure S11). EQE spectra of the tandem sub-cells are shown in Figure 4e. The integrated current densities of the organic sub-cells are 13.1, 13.3, and 12.8 mA cm^{-2} for those without Ag, $Ag_{0.5}$, and Ag_1, respectively, and of the perovskite sub-cell is 14.6 mA cm^{-2}. The differences between the calculated J_{SC} and the measured J_{SC} are within the acceptable error range of 5%. When comparing Ag_1 to no Ag on the calculated J_{SC}, we can see the decrease in organic sub-cell due to transparency loss, following the trend of the $J-V$ measurement as well as the simulated absorption profile of the back cell shown in Figure 4f (other layers in Figure S12).

Table 2. Tandem Photovoltaic Parameters of Three Different ICL Variations[a]

tandem devices	J_{SC} [mA cm^{-2}]	V_{OC} [V]	FF [%]	PCE [%]
without Ag	13.8 (13.9)	1.83 (1.75)	69.4 (67.2)	17.6 (16.2)
$Ag_{0.5}$	13.8 (13.7)	1.85 (1.77)	70.5 (66.7)	18.0 (16.2)
Ag_1	13.6 (13.5)	1.83 (1.76)	69.8 (68.6)	17.4 (16.4)

[a]Average values in parentheses calculated from 15 devices per variation.

We performed stability measurements of tandem devices under both solar simulation and outdoor conditions. Figure 5a shows the light-soaking stability performance of tandem devices with different ICLs under an inert atmosphere and under continuous full-spectrum illumination held at the maximum power point (MPP). The device parameter changes are shown in Figure S13. All tandems exhibit an initial burn-in within the first 100 h. However, after this initial period, a rather slower progression in PCE degradation is observed in the device with a metal-free ICL, followed by the $Ag_{0.5}$ and Ag_1 device, respectively. After 800 h of illumination, the Ag-free tandem retained 72% of its original PCE, compared to 36 and 27% for $Ag_{0.5}$ and Ag_1 ICL devices, respectively. To further investigate the reason for this stability enhancement in the metal-free ICL device, the photostability of organic single junctions was tested with a stack of ITO/SnO_2/different thicknesses of Ag layer/PEDOT:PSS/PTB7-Th:IEICO-4F/PFN-Br/Ag. As shown in Figure 5b, a similar trend in stability was observed in these single-junction devices, whereby the metal-free ICL cell demonstrated the highest stability, and the Ag_1-containing cell showed a steeped PCE decay. The device parameter changes are shown in Figure S14. From this study, we can conclude that the interaction between Ag and PEDOT:PSS, as reported elsewhere[50] is a major source of instability within tandem devices containing such an interlayer. Interestingly, the typical organic single-junction configuration, where PEDOT:PSS is deposited directly onto the glass/ITO, shows the worst photostability due to the corrosion of the ITO by the acidic nature of PEDOT:PSS.[51] Therefore, a generalized route to greater OPV stability may be to insert a thin SnO_2 layer between ITO and PEDOT:PSS. We performed our outdoor stability measurements (Figure 5c) on encapsulated single junction and tandem devices with Ag-free ICL in Thuwal, Saudi Arabia, with an average air temperature of 32 °C (Figure S15) for 15 consecutive days. The cells' max power point (MPP) was continuously tracked, with the power output normalized to the first day's peak as shown in Figure 5d. After 15 days in operation with no UV-filtering, the tandem devices retain 73% of its original power output, compared to 37 and 18% in the perovskite and organic single junctions, respectively. The large improvement in operational outdoor stability under real-world conditions highlights the unique benefit of perovskite/organic tandems over their constituent sub-cells. In tandem configuration, the perovskite front sub-cell is protected by the stack of ICL and the whole back cell from the diffusion of the top Ag electrode, whereas their single-junction counterpart has an Ag electrode separated from the perovskite only by thin layers of 7 nm C_{60}/3 nm BCP. Furthermore, the unfiltered near-UV irradiation adversely affects the longevity of the organic single junction by adding a detrimental chemical effect of PEDOT:PSS over the sputtered ITO electrode, as well as degrading on the photoactive layer itself. In the tandem configuration, the perovskite layer absorbs the near-UV irradiation and prevents it from reaching the organic active layer, and enhances the device lifetime.

https://doi.org/10.1021/acsaem.2c01749
ACS Appl. Energy Mater. 2022, 5, 14035−14044

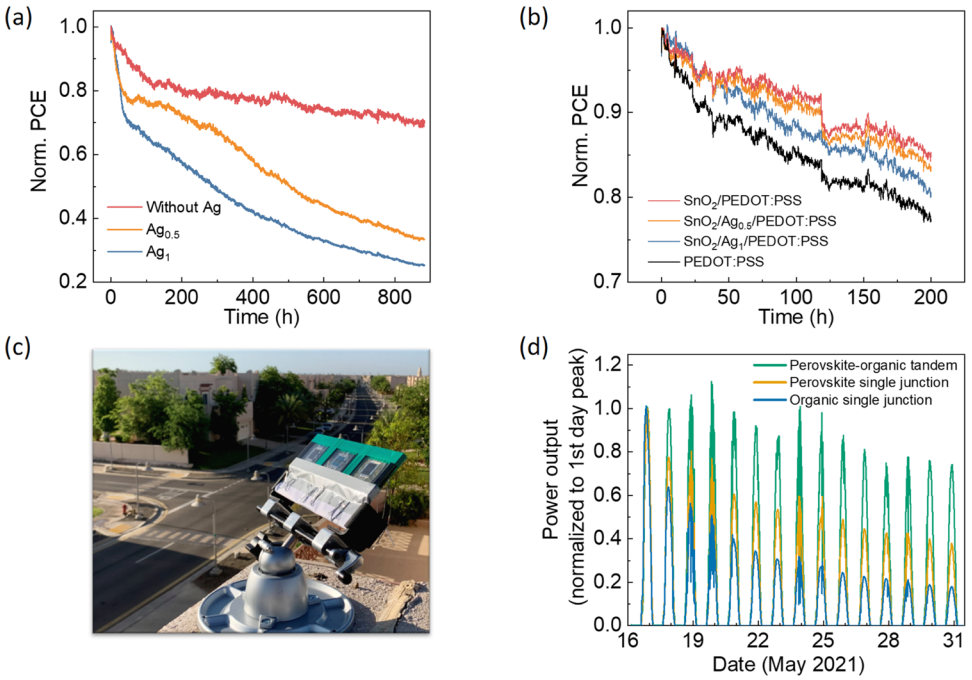

Figure 5. (a) Photostability test of the monolithic tandem devices with three different ICLs (without Ag, $Ag_{0.5}$, and Ag_1) held at MPP under an inert atmosphere and under continuous illumination. (b) Photostability test of the single-junction OSCs (ITO/anode interlayers/PTB7-Th:IEICO-4F/PFN-Br/Ag) run under an inert atmosphere and under continuous illumination. (c) Picture of the outdoor testing setup. (d) Outdoor stability with the normalized power output per day of the perovskite and organic single-junction devices as well as the Ag-free tandem device tested for 15 consecutive days.

4. CONCLUSIONS

In summary, we successfully developed a perovskite/organic monolithic tandem solar cell with a metal-free interconnecting layer. Such ICLs have unique advantages compared to the commonly employed Ag-containing ICLs. Owing to the negligible parasitic absorption, metal-free ICL tandem devices possess reduced optical losses and deliver higher J_{SC}. The removal of a time-consuming and energy-intensive vacuum deposition step in the tandem fabrication process simplifies the device fabrication with a minimal trade-off in photovoltaic performance. Furthermore, such devices enhance photostability by blocking the UV radiation for the organic back cell with the perovskite front cell. Under continuous illumination for 800 h, the metal-free ICL tandems demonstrate a dramatically increased photostability, retaining 72% of its initial PCE. Finally, we displayed the benefits of the tandem configuration under real-world conditions, where we highlight the improvement in operational stability over organic and perovskite single-junction cells. This finding paves the way for future innovations in perovskite/organic monolithic tandem photovoltaics to achieve application as stable and efficient devices.

■ ASSOCIATED CONTENT

Supporting Information

The Supporting Information is available free of charge at https://pubs.acs.org/doi/10.1021/acsaem.2c01749.

Additional experimental results and data (Figures S1–S15), including device characterization, absorption spectra, statistical photovoltaic parameters, optical simulation graphs, SEM images, KPFM, *n* and *k* values from ellipsometry measurement, and outdoor condition parameters (PDF)

■ AUTHOR INFORMATION

Corresponding Authors

Joel Troughton − *KAUST Solar Center (KSC), Physical Sciences and Engineering Division (PSE), King Abdullah University of Science and Technology (KAUST), Thuwal 23955-6900, Saudi Arabia*; Email: joel.troughton@kaust.edu.sa

Derya Baran − *KAUST Solar Center (KSC), Physical Sciences and Engineering Division (PSE), King Abdullah University of Science and Technology (KAUST), Thuwal 23955-6900, Saudi Arabia*; orcid.org/0000-0003-2196-8187; Email: derya.baran@kaust.edu.sa

Authors

Han Xu − *KAUST Solar Center (KSC), Physical Sciences and Engineering Division (PSE), King Abdullah University of Science and Technology (KAUST), Thuwal 23955-6900, Saudi Arabia*

Luis Torres Merino − *KAUST Solar Center (KSC), Physical Sciences and Engineering Division (PSE), King Abdullah University of Science and Technology (KAUST), Thuwal 23955-6900, Saudi Arabia*

Mehmet Koc − *ODTÜ GÜNAM, Middle East Technical University, 06800 Ankara, Turkey*; orcid.org/0000-0002-7524-0119

Erkan Aydin − *KAUST Solar Center (KSC), Physical Sciences and Engineering Division (PSE), King Abdullah University of Science and Technology (KAUST), Thuwal 23955-6900, Saudi Arabia*; orcid.org/0000-0002-8849-2788

Shynggys Zhumagali − *KAUST Solar Center (KSC), Physical Sciences and Engineering Division (PSE), King Abdullah University of Science and Technology (KAUST), Thuwal 23955-6900, Saudi Arabia*

https://doi.org/10.1021/acsaem.2c01749
ACS Appl. Energy Mater. 2022, 5, 14035−14044

Md Azimul Haque − *KAUST Solar Center (KSC), Physical Sciences and Engineering Division (PSE), King Abdullah University of Science and Technology (KAUST), Thuwal 23955-6900, Saudi Arabia;* orcid.org/0000-0003-3528-0674

Aren Yazmaciyan − *KAUST Solar Center (KSC), Physical Sciences and Engineering Division (PSE), King Abdullah University of Science and Technology (KAUST), Thuwal 23955-6900, Saudi Arabia*

Anirudh Sharma − *KAUST Solar Center (KSC), Physical Sciences and Engineering Division (PSE), King Abdullah University of Science and Technology (KAUST), Thuwal 23955-6900, Saudi Arabia;* orcid.org/0000-0003-4841-0108

Diego Rosas Villalva − *KAUST Solar Center (KSC), Physical Sciences and Engineering Division (PSE), King Abdullah University of Science and Technology (KAUST), Thuwal 23955-6900, Saudi Arabia;* orcid.org/0000-0001-7165-5256

Luis Huerta Hernandez − *KAUST Solar Center (KSC), Physical Sciences and Engineering Division (PSE), King Abdullah University of Science and Technology (KAUST), Thuwal 23955-6900, Saudi Arabia*

Michele De Bastiani − *KAUST Solar Center (KSC), Physical Sciences and Engineering Division (PSE), King Abdullah University of Science and Technology (KAUST), Thuwal 23955-6900, Saudi Arabia;* orcid.org/0000-0002-4870-2699

Maxime Babics − *KAUST Solar Center (KSC), Physical Sciences and Engineering Division (PSE), King Abdullah University of Science and Technology (KAUST), Thuwal 23955-6900, Saudi Arabia*

Furkan H. Isikgor − *KAUST Solar Center (KSC), Physical Sciences and Engineering Division (PSE), King Abdullah University of Science and Technology (KAUST), Thuwal 23955-6900, Saudi Arabia;* orcid.org/0000-0003-0787-7991

Stefaan De Wolf − *KAUST Solar Center (KSC), Physical Sciences and Engineering Division (PSE), King Abdullah University of Science and Technology (KAUST), Thuwal 23955-6900, Saudi Arabia;* orcid.org/0000-0003-1619-9061

Selcuk Yerci − *ODTÜ GÜNAM, Middle East Technical University, 06800 Ankara, Turkey; Electrical and Electronics Engineering, Middle East Technical University, 06800 Ankara, Turkey*

Complete contact information is available at: https://pubs.acs.org/10.1021/acsaem.2c01749

Author Contributions

[‖]H.X. and L.T.M. contributed equally to this paper.

Notes

The authors declare no competing financial interest.

■ ACKNOWLEDGMENTS

This publication is based upon work supported by the King Abdullah University of Science and Technology (KAUST) Office of Sponsored Research (OSR) under Award No. CCF-3079.

■ REFERENCES

(1) NREL. Best Research-Cell Efficiency Chart. https://www.nrel.gov/pv/cell-efficiency.html (accessed June 30, 2022).

(2) Shockley, W.; Queisser, H. J. Detailed Balance Limit of Efficiency of P-N Junction Solar Cells. *J. Appl. Phys.* **1961**, *32*, 510−519.

(3) Guillemoles, J.-F.; Kirchartz, T.; Cahen, D.; Rau, U. Guide for the Perplexed to the Shockley−Queisser Model for Solar Cells. *Nat. Photonics* **2019**, *13*, 501−505.

(4) Li, H.; Zhang, W. Perovskite Tandem Solar Cells: From Fundamentals to Commercial Deployment. *Chem. Rev.* **2020**, *120*, 9835−9950.

(5) Meng, L.; Wei, Z.; Zuo, T.; Gao, P. Finding Junction Partners for Cspbi3 in a Two-Terminal Tandem Solar Cell: A Theoretical Prospect. *Nano Energy* **2020**, *75*, No. 104866.

(6) Palmstrom, A. F.; Eperon, G. E.; Leijtens, T.; Prasanna, R.; Habisreutinger, S. N.; Nemeth, W.; Gaulding, E. A.; Dunfield, S. P.; Reese, M.; Nanayakkara, S.; Moot, T.; Werner, J.; Liu, J.; To, B.; Christensen, S. T.; McGehee, M. D.; van Hest, M. F. A. M.; Luther, J. M.; Berry, J. J.; Moore, D. T. Enabling Flexible All-Perovskite Tandem Solar Cells. *Joule* **2019**, *3*, 2193−2204.

(7) Chen, C.-W.; Hsiao, S.-Y.; Chen, C.-Y.; Kang, H.-W.; Huang, Z.-Y.; Lin, H.-W. Optical Properties of Organometal Halide Perovskite Thin Films and General Device Structure Design Rules for Perovskite Single and Tandem Solar Cells. *J. Mater. Chem. A* **2015**, *3*, 9152−9159.

(8) Marshall, K. P.; Walker, M.; Walton, R. I.; Hatton, R. A. Enhanced Stability and Efficiency in Hole-Transport-Layer-Free Cssni3 Perovskite Photovoltaics. *Nat. Energy* **2016**, *1*, 16178.

(9) Prasanna, R.; Leijtens, T.; Dunfield, S. P.; Raiford, J. A.; Wolf, E. J.; Swifter, S. A.; Werner, J.; Eperon, G. E.; de Paula, C.; Palmstrom, A. F.; Boyd, C. C.; van Hest, M. F. A. M.; Bent, S. F.; Teeter, G.; Berry, J. J.; McGehee, M. D. Design of Low Bandgap Tin−Lead Halide Perovskite Solar Cells to Achieve Thermal, Atmospheric and Operational Stability. *Nat. Energy* **2019**, *4*, 939−947.

(10) Werner, J.; Moot, T.; Gossett, T. A.; Gould, I. E.; Palmstrom, A. F.; Wolf, E. J.; Boyd, C. C.; van Hest, M. F. A. M.; Luther, J. M.; Berry, J. J.; McGehee, M. D. Improving Low-Bandgap Tin−Lead Perovskite Solar Cells Via Contact Engineering and Gas Quench Processing. *ACS Energy Lett.* **2020**, *5*, 1215−1223.

(11) Kapil, G.; Bessho, T.; Maekawa, T.; Baranwal, A. K.; Zhang, Y.; Kamarudin, M. A.; Hirotani, D.; Shen, Q.; Segawa, H.; Hayase, S. Tin-Lead Perovskite Fabricated Via Ethylenediamine Interlayer Guides to the Solar Cell Efficiency of 21.74%. *Adv. Energy Mater.* **2021**, *11*, No. 2101069.

(12) Wang, C.; Zhang, Y.; Gu, F.; Zhao, Z.; Li, H.; Jiang, H.; Bian, Z.; Liu, Z. Illumination Durability and High-Efficiency Sn-Based Perovskite Solar Cell under Coordinated Control of Phenylhydrazine and Halogen Ions. *Matter* **2021**, *4*, 709−721.

(13) Nishimura, K.; Kamarudin, M. A.; Hirotani, D.; Hamada, K.; Shen, Q.; Iikubo, S.; Minemoto, T.; Yoshino, K.; Hayase, S. Lead-Free Tin-Halide Perovskite Solar Cells with 13% Efficiency. *Nano Energy* **2020**, *74*, No. 104858.

(14) Chaturvedi, N.; Gasparini, N.; Corzo, D.; Bertrandie, J.; Wehbe, N.; Troughton, J.; Baran, D. All Slot-Die Coated Non-Fullerene Organic Solar Cells with Pce 11%. *Adv. Funct. Mater.* **2021**, *31*, No. 2009996.

(15) Zhao, H.; Naveed, H. B.; Lin, B.; Zhou, X.; Yuan, J.; Zhou, K.; Wu, H.; Guo, R.; Scheel, M. A.; Chumakov, A.; Roth, S. V.; Tang, Z.; Müller-Buschbaum, P.; Ma, W. Hot Hydrocarbon-Solvent Slot-Die Coating Enables High-Efficiency Organic Solar Cells with Temperature-Dependent Aggregation Behavior. *Adv. Mater.* **2020**, *32*, No. 2002302.

(16) Dong, S.; Jia, T.; Zhang, K.; Jing, J.; Huang, F. Single-Component Non-Halogen Solvent-Processed High-Performance Organic Solar Cell Module with Efficiency over 14%. *Joule* **2020**, *4*, 2004−2016.

(17) Li, N.; Baran, D.; Spyropoulos, G. D.; Zhang, H.; Berny, S.; Turbiez, M.; Ameri, T.; Krebs, F. C.; Brabec, C. J. Environmentally Printing Efficient Organic Tandem Solar Cells with High Fill Factors: A Guideline Towards 20% Power Conversion Efficiency. *Adv. Energy Mater.* **2014**, *4*, No. 1400084.

(18) Li, N.; Baran, D.; Forberich, K.; Turbiez, M.; Ameri, T.; Krebs, F. C.; Brabec, C. J. An Efficient Solution-Processed Intermediate Layer for Facilitating Fabrication of Organic Multi-Junction Solar Cells. *Adv. Energy Mater.* **2013**, *3*, 1597−1605.
(19) Song, X.; Gasparini, N.; Ye, L.; Yao, H.; Hou, J.; Ade, H.; Baran, D. Controlling Blend Morphology for Ultrahigh Current Density in Nonfullerene Acceptor-Based Organic Solar Cells. *ACS Energy Lett.* **2018**, *3*, 669−676.
(20) Troughton, J.; Neubert, S.; Gasparini, N.; Villalva, D. R.; Bertrandie, J.; Seitkhan, A.; Paleti, S. H. K.; Sharma, A.; De Bastiani, M.; Aydin, E.; Anthopoulos, T. D.; De Wolf, S.; Schlatmann, R.; Baran, D. Efficient Hybrid Amorphous Silicon/Organic Tandem Solar Cells Enabled by near-Infrared Absorbing Nonfullerene Acceptors. *Adv. Energy Mater.* **2021**, *11*, No. 2100166.
(21) Yuan, J.; Zhang, Y.; Zhou, L.; Zhang, G.; Yip, H.-L.; Lau, T.-K.; Lu, X.; Zhu, C.; Peng, H.; Johnson, P. A.; Leclerc, M.; Cao, Y.; Ulanski, J.; Li, Y.; Zou, Y. Single-Junction Organic Solar Cell with over 15% Efficiency Using Fused-Ring Acceptor with Electron-Deficient Core. *Joule* **2019**, *3*, 1140−1151.
(22) Cui, Y.; Yao, H.; Zhang, J.; Xian, K.; Zhang, T.; Hong, L.; Wang, Y.; Xu, Y.; Ma, K.; An, C.; He, C.; Wei, Z.; Gao, F.; Hou, J. Single-Junction Organic Photovoltaic Cells with Approaching 18% Efficiency. *Adv. Mater.* **2020**, *32*, No. 1908205.
(23) Lee, J.; Ko, S.-J.; Seifrid, M.; Lee, H.; Luginbuhl, B. R.; Karki, A.; Ford, M.; Rosenthal, K.; Cho, K.; Nguyen, T.-Q.; Bazan, G. C. Bandgap Narrowing in Non-Fullerene Acceptors: Single Atom Substitution Leads to High Optoelectronic Response Beyond 1000 Nm. *Adv. Energy Mater.* **2018**, *8*, No. 1801212.
(24) Yao, H.; Cui, Y.; Yu, R.; Gao, B.; Zhang, H.; Hou, J. Design, Synthesis, and Photovoltaic Characterization of a Small Molecular Acceptor with an Ultra-Narrow Band Gap. *Angew. Chem., Int. Ed.* **2017**, *56*, 3045−3049.
(25) Han, Y.; Dong, H.; Pan, W.; Liu, B.; Chen, X.; Huang, R.; Li, Z.; Li, F.; Luo, Q.; Zhang, J.; Wei, Z.; Ma, C.-Q. An Efficiency of 16.46% and a T80 Lifetime of over 4000 H for the Pm6:Y6 Inverted Organic Solar Cells Enabled by Surface Acid Treatment of the Zinc Oxide Electron Transporting Layer. *ACS Appl. Mater. Interfaces* **2021**, *13*, 17869−17881.
(26) Jiang, B.-H.; Wang, Y.-P.; Su, Y.-W.; Chang, J.-F.; Chueh, C.-C.; Shen, M.-H.; Shieh, T.-S.; Jeng, R.-J.; Chen, C.-P. Realizing Stable High-Performance and Low-Energy-Loss Ternary Photovoltaics through Judicious Selection of the Third Component. *Sol. RRL* **2021**, *5*, No. 2100450.
(27) Zhu, Y.; Gadisa, A.; Peng, Z.; Ghasemi, M.; Ye, L.; Xu, Z.; Zhao, S.; Ade, H. Rational Strategy to Stabilize an Unstable High-Efficiency Binary Nonfullerene Organic Solar Cells with a Third Component. *Adv. Energy Mater.* **2019**, *9*, No. 1900376.
(28) Xu, X.; Xiao, J.; Zhang, G.; Wei, L.; Jiao, X.; Yip, H.-L.; Cao, Y. Interface-Enhanced Organic Solar Cells with Extrapolated T80 Lifetimes of over 20 Years. *Sci. Bull.* **2020**, *65*, 208−216.
(29) Li, Y.; Huang, X.; Ding, K.; Sheriff, H. K. M.; Ye, L.; Liu, H.; Li, C.-Z.; Ade, H.; Forrest, S. R. Non-Fullerene Acceptor Organic Photovoltaics with Intrinsic Operational Lifetimes over 30 Years. *Nat. Commun.* **2021**, *12*, No. 5419.
(30) Chen, X.; Jia, Z.; Chen, Z.; Jiang, T.; Bai, L.; Tao, F.; Chen, J.; Chen, X.; Liu, T.; Xu, X.; Yang, C.; Shen, W.; Sha, W. E. I.; Zhu, H.; Yang, Y. Efficient and Reproducible Monolithic Perovskite/Organic Tandem Solar Cells with Low-Loss Interconnecting Layers. *Joule* **2020**, *4*, 1594−1606.
(31) Lang, K.; Guo, Q.; He, Z.; Bai, Y.; Yao, J.; Wakeel, M.; Alhodaly, M. S.; Hayat, T.; Tan, Za. High Performance Tandem Solar Cells with Inorganic Perovskite and Organic Conjugated Molecules to Realize Complementary Absorption. *J. Phys. Chem. Lett.* **2020**, *11*, 9596−9604.
(32) Xie, S.; Xia, R.; Chen, Z.; Tian, J.; Yan, L.; Ren, M.; Li, Z.; Zhang, G.; Xue, Q.; Yip, H.-L.; Cao, Y. Efficient Monolithic Perovskite/Organic Tandem Solar Cells and Their Efficiency Potential. *Nano Energy* **2020**, *78*, No. 105238.
(33) Liu, L.; Xiao, Z.; Zuo, C.; Ding, L. Inorganic Perovskite/Organic Tandem Solar Cells with Efficiency over 20%. *J. Semicond.* **2021**, *42*, No. 020501.
(34) Wu, X.; Liu, Y.; Qi, F.; Lin, F.; Fu, H.; Jiang, K.; Wu, S.; Bi, L.; Wang, D.; Xu, F.; Jen, A. K. Y.; Zhu, Z. Improved Stability and Efficiency of Perovskite/Organic Tandem Solar Cells with an All-Inorganic Perovskite Layer. *J. Mater. Chem. A* **2021**, *9*, 19778−19787.
(35) Chen, W.; Zhu, Y.; Xiu, J.; Chen, G.; Liang, H.; Liu, S.; Xue, H.; Birgersson, E.; Ho, J. W.; Qin, X.; Lin, J.; Ma, R.; Liu, T.; He, Y.; Ng, A. M.-C.; Guo, X.; He, Z.; Yan, H.; Djurišić, A. B.; Hou, Y. Monolithic Perovskite/Organic Tandem Solar Cells with 23.6% Efficiency Enabled by Reduced Voltage Losses and Optimized Interconnecting Layer. *Nat. Energy* **2022**, *7*, 229−237.
(36) Qin, S.; Lu, C.; Jia, Z.; Wang, Y.; Li, S.; Lai, W.; Shi, P.; Wang, R.; Zhu, C.; Du, J.; Zhang, J.; Meng, L.; Li, Y. Constructing Monolithic Perovskite/Organic Tandem Solar Cell with Efficiency of 22.0% Via Reduced Open-Circuit Voltage Loss and Broadened Absorption Spectra. *Adv. Mater.* **2022**, *34*, No. 2108829.
(37) Li, C.; Wang, Y.; Choy, W. C. H. Efficient Interconnection in Perovskite Tandem Solar Cells. *Small Methods* **2020**, *4*, No. 2000093.
(38) Yin, Z.; Wei, J.; Zheng, Q. Interfacial Materials for Organic Solar Cells: Recent Advances and Perspectives. *Adv. Sci.* **2016**, *3*, No. 1500362.
(39) Lu, S.; Ouyang, D.; Choy, W. C. Recent Progress of Interconnecting Layer for Tandem Organic Solar Cells. *Sci. China: Chem.* **2017**, *60*, 460−471.
(40) Ko, Y.; Park, H.; Lee, C.; Kang, Y.; Jun, Y. Recent Progress in Interconnection Layer for Hybrid Photovoltaic Tandems. *Adv. Mater.* **2020**, *32*, No. 2002196.
(41) Zhao, D.; Chen, C.; Wang, C.; Junda, M. M.; Song, Z.; Grice, C. R.; Yu, Y.; Li, C.; Subedi, B.; Podraza, N. J.; Zhao, X.; Fang, G.; Xiong, R.-G.; Zhu, K.; Yan, Y. Efficient Two-Terminal All-Perovskite Tandem Solar Cells Enabled by High-Quality Low-Bandgap Absorber Layers. *Nat. Energy* **2018**, *3*, 1093−1100.
(42) Tong, J.; Song, Z.; Kim, D. H.; Chen, X.; Chen, C.; Palmstrom, A. F.; Ndione, P. F.; Reese, M. O.; Dunfield, S. P.; Reid, O. G.; Liu, J.; Zhang, F.; Harvey, S. P.; Li, Z.; Christensen, S. T.; Teeter, G.; Zhao, D.; Al-Jassim, M. M.; van Hest, M. F. A. M.; Beard, M. C.; Shaheen, S. E.; Berry, J. J.; Yan, Y.; Zhu, K. Carrier Lifetimes of ≫1 Ms in Sn-Pb Perovskites Enable Efficient All-Perovskite Tandem Solar Cells. *Science* **2019**, *364*, 475−479.
(43) Lin, R.; Xiao, K.; Qin, Z.; Han, Q.; Zhang, C.; Wei, M.; Saidaminov, M. I.; Gao, Y.; Xu, J.; Xiao, M.; Li, A.; Zhu, J.; Sargent, E. H.; Tan, H. Monolithic All-Perovskite Tandem Solar Cells with 24.8% Efficiency Exploiting Comproportionation to Suppress Sn(Ii) Oxidation in Precursor Ink. *Nat. Energy* **2019**, *4*, 864−873.
(44) Koc, M.; Ameri, M.; Yerci, S. Optical Design of Tco-Free Interconnecting Layer for All-Perovskite Tandem Solar Cells. *Appl. Phys. Lett.* **2021**, *119*, No. 021102.
(45) De Bastiani, M.; Subbiah, A. S.; Aydin, E.; Isikgor, F. H.; Allen, T. G.; De Wolf, S. Recombination Junctions for Efficient Monolithic Perovskite-Based Tandem Solar Cells: Physical Principles, Properties, Processing and Prospects. *Mater. Horiz.* **2020**, *7*, 2791−2809.
(46) Brinkmann, K. O.; Gahlmann, T.; Riedl, T. Atomic Layer Deposition of Functional Layers in Planar Perovskite Solar Cells. *Sol. RRL* **2020**, *4*, No. 1900332.
(47) Yu, Z.; Yang, Z.; Ni, Z.; Shao, Y.; Chen, B.; Lin, Y.; Wei, H.; Yu, Z. J.; Holman, Z.; Huang, J. Simplified Interconnection Structure Based on C60/Sno2-X for All-Perovskite Tandem Solar Cells. *Nat. Energy* **2020**, *5*, 657−665.
(48) Wang, J.; Zardetto, V.; Datta, K.; Zhang, D.; Wienk, M. M.; Janssen, R. A. J. 16.8% Monolithic All-Perovskite Triple-Junction Solar Cells Via a Universal Two-Step Solution Process. *Nat. Commun.* **2020**, *11*, No. 5254.
(49) Xiao, K.; Lin, R.; Han, Q.; Hou, Y.; Qin, Z.; Nguyen, H. T.; Wen, J.; Wei, M.; Yeddu, V.; Saidaminov, M. I.; Gao, Y.; Luo, X.; Wang, Y.; Gao, H.; Zhang, C.; Xu, J.; Zhu, J.; Sargent, E. H.; Tan, H. All-Perovskite Tandem Solar Cells with 24.2% Certified Efficiency and

https://doi.org/10.1021/acsaem.2c01749
ACS Appl. Energy Mater. 2022, 5, 14035−14044

Area over 1 Cm2 Using Surface-Anchoring Zwitterionic Antioxidant. *Nat. Energy* **2020**, *5*, 870−880.
(50) Choi, D. Y.; Kang, H. W.; Sung, H. J.; Kim, S. S. Annealing-Free, Flexible Silver Nanowire−Polymer Composite Electrodes Via a Continuous Two-Step Spray-Coating Method. *Nanoscale* **2013**, *5*, 977−983.
(51) Meng, Y.; Hu, Z.; Ai, N.; Jiang, Z.; Wang, J.; Peng, J.; Cao, Y. Improving the Stability of Bulk Heterojunction Solar Cells by Incorporating Ph-Neutral Pedot:Pss as the Hole Transport Layer. *ACS Appl. Mater. Interfaces* **2014**, *6*, 5122−5129.
(52) Brinkmann, K. O.; Becker, T.; Zimmermann, F.; Kreusel, C.; Gahlmann, T.; Theisen, M.; Haeger, T.; Olthof, S.; Tückmantel, C.; Günster, M.; Maschwitz, T.; Göbelsmann, F.; Koch, C.; Hertel, D.; Caprioglio, P.; Peña-Camargo, F.; Perdigón-Toro, L.; Al-Ashouri, A.; Merten, L.; Hinderhofer, A.; Gomell, L.; Zhang, S.; Schreiber, F.; Albrecht, S.; Meerholz, K.; Neher, D.; Stolterfoht, M.; Riedl, T. Perovskite−Organic Tandem Solar Cells with Indium Oxide Interconnect. *Nature* **2022**, *604*, 280−286.
(53) Turren-Cruz, S.-H.; Hagfeldt, A.; Saliba, M. Methylammonium-Free, High-Performance, and Stable Perovskite Solar Cells on a Planar Architecture. *Science* **2018**, *362*, 449−453.
(54) Classen, A.; Heumueller, T.; Wabra, I.; Gerner, J.; He, Y.; Einsiedler, L.; Li, N.; Matt, G. J.; Osvet, A.; Du, X.; Hirsch, A.; Brabec, C. J. Revealing Hidden Uv Instabilities in Organic Solar Cells by Correlating Device and Material Stability. *Adv. Energy Mater.* **2019**, *9*, No. 1902124.
(55) Jørgensen, M.; Norrman, K.; Gevorgyan, S. A.; Tromholt, T.; Andreasen, B.; Krebs, F. C. Stability of Polymer Solar Cells. *Adv. Mater.* **2012**, *24*, 580−612.
(56) Chen, W.; Zhang, J.; Xu, G.; Xue, R.; Li, Y.; Zhou, Y.; Hou, J.; Li, Y. A Semitransparent Inorganic Perovskite Film for Overcoming Ultraviolet Light Instability of Organic Solar Cells and Achieving 14.03% Efficiency. *Adv. Mater.* **2018**, *30*, No. 1800855.
(57) Jošt, M.; Kegelmann, L.; Korte, L.; Albrecht, S. Monolithic Perovskite Tandem Solar Cells: A Review of the Present Status and Advanced Characterization Methods toward 30% Efficiency. *Adv. Energy Mater.* **2020**, *10*, No. 1904102.
(58) Leijtens, T.; Bush, K. A.; Prasanna, R.; McGehee, M. D. Opportunities and Challenges for Tandem Solar Cells Using Metal Halide Perovskite Semiconductors. *Nat. Energy* **2018**, *3*, 828−838.
(59) Al-Ashouri, A.; Köhnen, E.; Li, B.; Magomedov, A.; Hempel, H.; Caprioglio, P.; Márquez, J. A.; Morales Vilches, A. B.; Kasparavicius, E.; Smith, J. A.; Phung, N.; Menzel, D.; Grischek, M.; Kegelmann, L.; Skroblin, D.; Gollwitzer, C.; Malinauskas, T.; Jošt, M.; Matič, G.; Rech, B.; Schlatmann, R.; Topič, M.; Korte, L.; Abate, A.; Stannowski, B.; Neher, D.; Stolterfoht, M.; Unold, T.; Getautis, V.; Albrecht, S. Monolithic Perovskite/Silicon Tandem Solar Cell with ≫29% Efficiency by Enhanced Hole Extraction. *Science* **2020**, *370*, 1300−1309.
(60) Koç, M.; Soltanpoor, W.; Bektaş, G.; Bolink, H. J.; Yerci, S. Guideline for Optical Optimization of Planar Perovskite Solar Cells. *Adv. Opt. Mater.* **2019**, *7*, No. 1900944.

https://doi.org/10.1021/acsaem.2c01749
ACS Appl. Energy Mater. 2022, 5, 14035−14044